ChemCatChem

Research Article
doi.org/10.1002/cctc.202400329

Chemistry Europe
European Chemical Societies Publishing

www.chemcatchem.org

N_2O Assisted Ethane Transformation into Ethylene Using $NiO–CeO_2–ZrO_2$ Catalysts

Ginebra Sánchez,[a] Ana M. Dejoz,[a] Ramón Fernández-Domene,[a] Isabel Barroso-Martín,[b] Daniel Ballesteros-Plata,[b] Antonia Infantes-Molina,[b] Juan A. Cecilia,*[b] Enrique Rodríguez-Castellón,[b] José M. López Nieto,*[c] Rita Sánchez-Tovar,[a] and Benjamín Solsona*[a]

$NiO–CeO_2$ and $NiO–CeO_2–ZrO_2$ catalysts have been synthesized, electrochemically characterized (Mott-Schottky (MS) measurements and Electrochemical Impedance Spectroscopy), physicochemically characterized (by N_2 adsorption, XRD, Transmission Electron Microscopy and XPS) and tested in the N_2O assisted ethane oxydehydrogenation. The use of low Zr-loadings (Zr/Ce = 0.1 at. ratio) has led to the optimal results in the ethylene production, improving those obtained by the Zr-free $NiO–CeO_2$ catalyst. However, high Zr-loadings have meant a decrease in the olefin production. The catalytic results obtained have been explained considering the amount of oxygen vacancies, the crystalline phases formed and, especially, the nature of the surface Ni species. Importantly, the use of N_2O as an oxidizing agent leads to a remarkable improvement in the selectivity to the olefin compared to that obtained employing molecular O_2. Then, for a given ethane conversion the selectivity to ethylene is ca. 15 points higher using N_2O than using O_2. Another additional positive aspect of this $NiO–CeO_2–ZrO_2$ catalyst is its high catalytic stability.

Introduction

Although N_2O is naturally present in the atmosphere as a part of the natural Earth's nitrogen cycle, around 40% of its emissions are directly derived from the human activity. Consequently, the concentration of N_2O in the atmosphere has increased 15–20% from the pre-industrial era until reaching nowadays ca. 330 ppb.[1] Unfortunately, N_2O is a powerful greenhouse gas. Then, although its overall contribution to the global warming (ca. 7%)[1] is lower than that of carbon dioxide and methane, its potential per molecule is remarkably higher (around 330 times higher than that of CO_2). Most of man-related N_2O emissions are related to the use of nitrogenated fertilizers but also to the burning of fuels, the production of HNO_3, the synthesis of adipic acid and the treatment of domestic wastewater.[2]

Then, different ways to diminish the level of the anthropogenic N_2O emissions have been proposed:

- Maximize the efficiency in the economic sectors that emit nitrous oxide the most
- Strictly control the N_2O losses (agriculture, industry, fuel combustion…)
- Minimize the N_2O formation (through a drastic technological improvement)
- Decompose N_2O by transforming it into molecular oxygen and nitrogen (N_2O abatement)
- Use of N_2O as a reactant in useful reactions (i.e. as a mild oxidizing agent).

Although it has been known for years,[3] the employment of N_2O as an oxidizing agent has attracted increased attention during the past years due not only to its close relationship with the global warming but also because its mild oxidizing character can mitigate undesired total oxidation reactions.[4–6]

NiO is a metal oxide that, generally, presents as a catalyst high reactivity in reactions that take place through a redox Mars-Van Krevelen mechanism. Unfortunately, in many cases this high catalytic activity is directed towards the formation of undesired reaction products, such as CO_2.[7–9] Interestingly, the strict control of the NiO preparation procedure[10,11] or the addition of suitable promoters and supports[12–15] can minimize the production of carbon oxides and promote the formation of high value products. This is the case of the transformation of ethane into ethylene using molecular oxygen by the oxidative

[a] G. Sánchez, A. M. Dejoz, R. Fernández-Domene, R. Sánchez-Tovar, B. Solsona
Department of Chemical Engineering, University de València, Av. Universitats s/n, 46100 Burjassot, Spain
E-mail: Benjamin.solsona@uv.es

[b] I. Barroso-Martín, D. Ballesteros-Plata, A. Infantes-Molina, J. A. Cecilia, E. Rodríguez-Castellón
Department of Inorganic Chemistry, Crystallography, and Mineralogy, Faculty of Sciences, University of Málaga, Campus de Teatinos, 29071 Málaga, Spain
E-mail: Jacecilia@uma.es

[c] J. M. López Nieto
Instituto de Tecnología Química, Universitat Politècnica de València-Consejo Superior de Investigaciones Científicas, Avenida de los Naranjos s/n, 46022 Valencia, Spain
E-mail: jmlopez@itq.upv.es
jmlopez@itq.upv.es

Supporting information for this article is available on the WWW under https://doi.org/10.1002/cctc.202400329

dehydrogenation (ODH) of ethane. The use of cerium oxide together with NiO is expected to increase the reactivity of the pure oxides since the presence of heteroatoms such as cerium could favour the formation of smaller crystallites and, therefore, to increase the amount of catalytic active sites.[16,17] Moreover, ceria presents a high oxygen storage capacity being able to change easily of oxidation states, i.e., Ce^{3+}–Ce^{4+}, then favouring reactions that follow redox mechanisms.[18–24] Additionally, in the ODH of ethane, an enhanced selectivity to ethylene has been also reported[25] for Ce–Ni–O catalysts if compared to both pure NiO or pure CeO_2. This fact has been linked to a faster diffusion of oxygen into the bulk when cerium is added to nickel oxide as well as a decrease in the amount of unselective highly oxidized surface oxygen species.

On the other hand, the N_2O decomposition to N_2 and O_2 is a widely studied reaction[26–28] that achieves the best results when noble metal-based catalysts are employed. However, some non-noble metal oxides exhibit comparable reactivity with the additional advantage of presenting a lower cost and a higher availability.[29,30] Among these oxides NiO is one of the most active together with Co_3O_4 or CuO.[31–34] Interestingly, NiO is a more robust oxide as tolerates certain amounts of oxygen, mitigating the decrease of reactivity.[35] The addition of NiO to an oxide as CeO_2 with high oxygen storage capacity (OSC) can even improve further both the activity and also the tolerance to non-ideal feeds. Then, an important synergistic effect between cerium and nickel takes place,[35–37] the role of Ce being the facilitation of the N_2O dissociation. On the other hand, it has been often reported that the incorporation of small amounts of Zr into the CeO_2 lattice leads to a drastic increase in the amount of oxygen vacancies compared to pure CeO_2[38–40] thus affecting its catalytic characteristics. Then, as one of the advantages of supporting nickel oxide on ceria lies on its high OSC, we have thought that the simultaneous addition of certain amounts of Zr and Ce could improve further the catalytic performance.

The ODH of ethane assisted by N_2O has been reported using catalysts with different compositions, mainly containing vanadium and iron.[41–43] Surprisingly, nickel oxide-based catalysts, which is one of the most efficient catalysts for the ODH of ethane with molecular oxygen, has been hardly studied. Ni–Al mixed oxides derived from layered double hydroxides as well as supported NiO/Al_2O_3 catalysts have been tested in the ODH-N_2O reaction.[44] The intensity of the adsorption as well as the concentration of O^- species were related to the catalytic performance.

In the present article, we show a combined reaction in which both the selective transformation of ethane and the decomposition of N_2O must take place simultaneously. The oxidative dehydrogenation of ethane on nickel oxide-based catalysts has been reported to take place through a redox MVK mechanism. Similarly, the same type of mechanism controls the N_2O decomposition to O_2 and N_2. Importantly, NiO-doped CeO_2 catalysts have been shown as efficient for both individual reactions (ODH-O_2 of ethane and the N_2O decomposition).

Therefore, in the present article we have studied the oxidative dehydrogenation of ethane to ethylene with N_2O as an oxidizing agent using NiO–CeO_2 and NiO–CeO_2–ZrO_2 catalysts, prepared by coprecipitation, in which the effect of the partial replacement of Ce^{4+} by Zr^{4+} has been also studied.

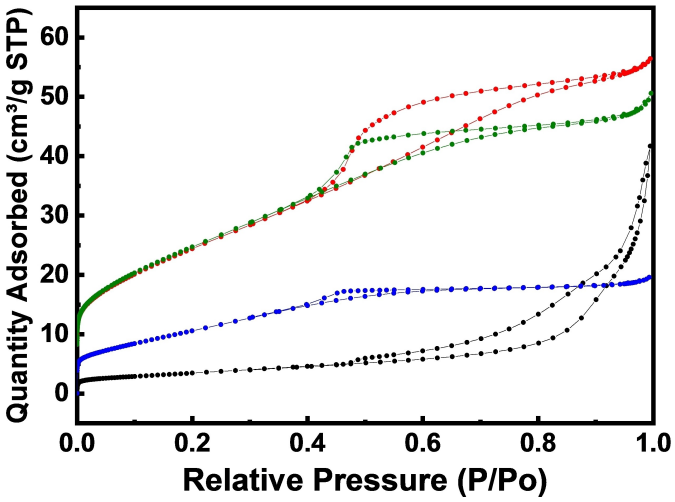

Figure 1. N_2 adsorption-desorption isotherms for the as-prepared samples: (**Black**) NiO, (Red) Ni–Ce, (Green) Ni-$Ce_{0.9}Zr_{0.1}$, (Blue) Ni-$Ce_{0.5}Zr_{0.5}$.

Results and Discussion

Characterization of Catalysts

Catalysts containing Ni, Ce and Zr (Zr/Ce at. ratios of 0.05, 0.1, 0.25 and 0.5) have been prepared, characterized by several physicochemical techniques and tested in the N_2O assisted ODH of ethane. Table 1 summarizes the main characterization results.

Figure 1 displays N_2 adsorption-desorption isotherms for the Ni–Ce–Zr–O samples as well as for one catalyst containing only nickel oxide (reference catalyst). The latter presented a type IV isotherm with a hysteresis loop due to capillary condensation,

Table 1. Textural properties of representative NiO–CeO_2 and NiO–CeO_2–ZrO_2 samples.

Catalyst	Ni/Ce/Zr Bulk at.	S_{BET} ($m^2 g^{-1}$)	S_{ext} ($m^2 g^{-1}$)	S_{micro} ($m^2 g^{-1}$)	S_{micro}/S_{total} (%)	Pore volume ($cm^3 g^{-1}$)
NiO	1/0/0	12				0.04
Ni–Ce	1/9/0	90	83	7	8	0.08
Ni–$Ce_{0.9}Zr_{0.1}$	1/8.1/0.9	91	71	20	22	0.07
Ni–$Ce_{0.5}Zr_{0.5}$	1/4.5/4.5	39	24	15	38	0.03

which is typical of conical and cylindrical mesopores closed at the tapered end. The sharp knee at low relative pressure ranges is attributed to the monolayer coverage.[45] The specific surface area calculated by BET method is 12 $m^2 g^{-1}$, with total pore volume of 0.035 $cm^3 g^{-1}$. NLDFT (Non-Local density functional theory) method was used to calculate pore size, indicating the presence of 125–250 Å mesopores. The H3 hysteresis loop is typical of materials with aggregates and platelet particles forming slit-shaped pores.[46] The rest of the samples showed a similar type IV isotherm but with a H2(b) hysteresis loop characteristic of mesoporous materials with a large distribution of neck widths and also indicative of pore blocking, as previously reported for CeNi oxide systems.[47] It is also observed that the addition of Zr provoked a considerable decrease in specific surface area and pore volume, ranging from 90 to 39 $m^2 g^{-1}$ in the sample with the highest Zr loading (see Table 1). In fact, the final saturation plateau is related to the complete filling of mesopores thus limiting the uptake at high relative pressures.

Regarding the pore size distribution (Figure 2), all prepared samples containing Ni, Ce and Zr presented a unimodal pore size distribution of narrow mesopores according to NLDFT method, with an average pore size of 35 Å, and the distribution becoming narrower as the amount of Zr increases. Then, it is observed that the S_{micro} increases with the Zr content, also detected by the isotherm profile.

The XRD patterns of the prepared catalysts as well as those for the reference oxides of Ce, Zr and CeZr are displayed in Figure 3. Ni–Ce sample shows the presence of cubic CeO_2 evidenced by the characteristic diffraction peaks at $2\theta = 28.6$, 33.1, 47.6, 56.4 and 59.2° (JCPDS: 03–065-5923). No diffraction peaks of other phases were detected. Regarding the diffraction of nickel phases, the relatively low metal loading hindered the identification of crystalline NiO in the prepared samples, although it is also indicative of a high dispersion of nickel sites on the surface of the catalysts, as will be shown below by EDX-STEM mapping. The same diffraction peaks were also evidenced for other samples after Zr incorporation although slightly shifted, mainly in the case of the sample with the highest Zr content. In this regard, the ***a*** unit cell parameter was calculated for Ni–Ce and Ni–$Ce_{0.9}Zr_{0.1}$ samples using CeO_2 (111) crystalline plane with values of 5.42 Å and 5.40 Å, respectively. The diminishing in ***a*** value suggests the introduction of Zr^{4+} cations into de CeO_2 structure, since Zr^{4+} ionic radius is smaller than that of Ce^{4+} counterpart (0.84 Å for Zr^{4+} vs 0.97 Å for Ce^{4+} [48]).[49] In the case of Ni–$Ce_{0.5}Zr_{0.5}$ sample, the main peak is found at higher value of 2θ, which is in accordance with the main peak of $Ce_{0.5}Zr_{0.5}O_2$ oxide, evidencing the formation of a Ce–Zr–O solid solution by coprecipitation in which the interplanar spacing of the Ce–Zr–O solid solution becomes bigger, as previously reported by other authors.[50,51] The calculated **a** unit cell parameter for Ni/$Ce_{0.5}Zr_{0.5}$ was 3.76 Å, which is close to that reported for the mixed oxide (3.72 Å, $Ce_{0.5}Zr_{0.5}O_2$, JCPDS: 00–038-1436), thus confirming the presence

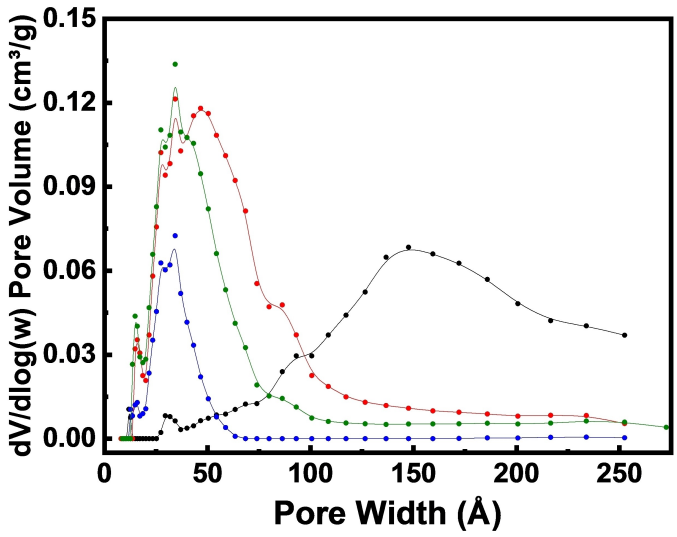

Figure 2. DFT pore size distribution of representative catalysts: (Black) NiO, Red) Ni/Ce, (Green) Ni/$Ce_{0.9}Zr_{0.1}$, (Blue) Ni/$Ce_{0.5}Zr_{0.5}$.

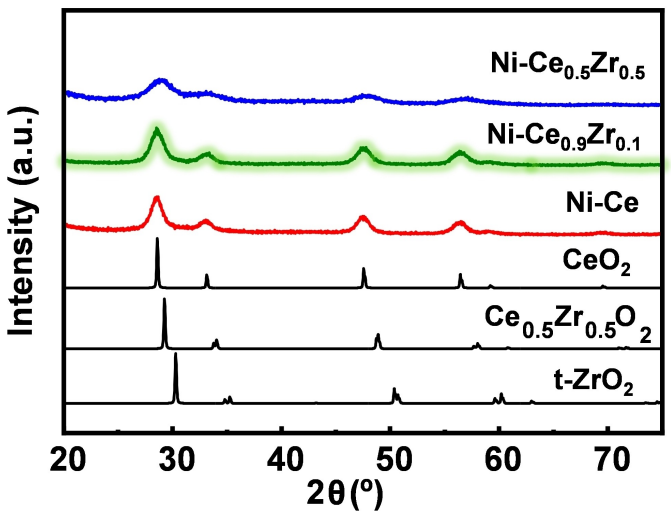

Figure 3. X-Ray diffractograms for the prepared Ni/CeZr samples and the reference patterns for CeO_2, ZrO_2 and CeZr mixed oxide.

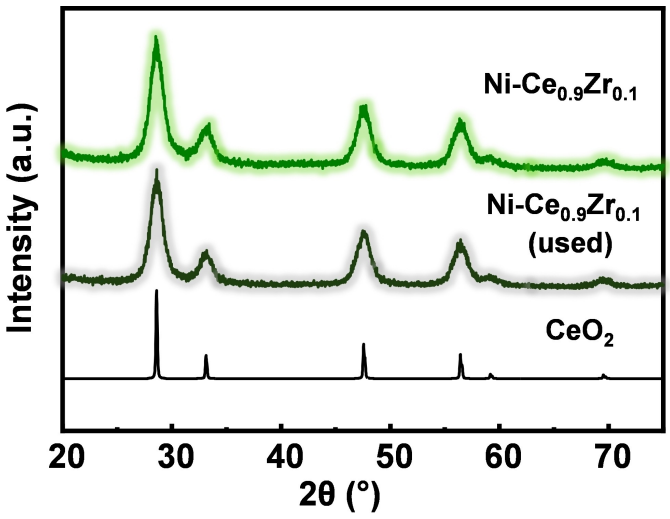

Figure 4. XRD patterns for fresh and used Ni–$Ce_{0.9}Zr_{0.1}$ and pure CeO_2 as reference.

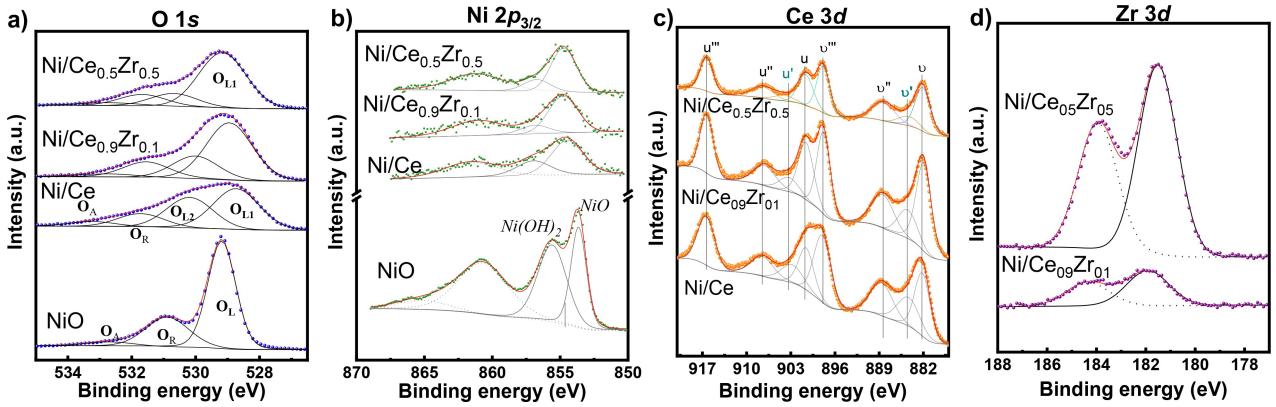

Figure 5. (a) O 1s, (b) Ni $2p_{3/2}$, (c) Ce 3*d* and (d) Zr 3*d* core level spectra for Ni–CeO_2–ZrO_2. For comparison the spectra related to pure NiO have been also included.

of the Ce–Zr–O solid solution. The broadness of the peaks could be indicative of this phase with low crystallinity. Diffraction peaks of ZrO_2 were not detected, suggesting either the absence of this crystalline phase and/or its amorphous character.

X-Ray diffraction was also performed for the most active/selective catalyst, Ni–$Ce_{0.9}Zr_{0.1}$, after reaction (see Figure 4). Interestingly, the catalyst did not present significant changes in its crystalline structure or the crystallite size before and after the catalytic test. This is in accordance with the stable behaviour observed during the ODH-N_2O assays, as will be shown later.

Information related to the near surface of the prepared samples was provided by XPS. The analysis of O 1s core level signal for all catalysts is depicted in Figure 5a. It is also included, for comparative purposes, that of pure NiO used as a reference catalyst. Pure NiO showed an unique pattern, which could be deconvoluted into three contributions. The main one at 529.1 eV can be related to lattice oxygen in NiO. A second one at 530.9 eV could be attributed to oxygen deficient regions, in agreement with NiO and $Ni(OH)_2$ species.[52,53] Finally, the last one at 532 eV can be related to hydroxyl groups on the catalysts' surface and oxygen vacancies with adsorbed surface oxygen species.[54] On the other hand, the samples containing Ce present a different profile and four clear contributions are noticeable. In this sense, Ni/Ce sample shows lattice oxygen contribution at 529.0 eV[55] (O_{L1}). The contribution at 530.1 eV (O_{L2}) indicates the presence of lattice oxygen with a more covalent nature, i.e., O^{2-} anions bonded to Ni or Ce, as previously reported for Ni-based catalysts supported on Ce–Zr–O.[51] Besides, two contributions at 531.7 eV and 533.0 eV are also present due to surface reactive oxygen (O_R) species such as O_2^{2-}/O^- adsorbed on oxygen vacancies on the surface (O_V) and surface adsorbed water (O_A),[56] respectively. Therefore, O_R stands for the amount of surface oxygen vacancies (O_V). In the catalysts containing zirconium, some differences are observed. Then, the incorporation of Zr^{4+} provokes a shift of the O lattice signals to higher values, justified by Zr incorporation into CeO_2 lattice as observed from XRD. Table 2 shows the contribution of each oxygen species to the total spectra for

Table 2. Surface oxygen species percentages (%) for the prepared catalysts determined by XPS.

Catalyst	O_{L1}	O_{L2}	O_L	O_R
Ni–Ce	49.4	35.4	84.8	15.3
Ni–$Ce_{0.9}Zr_{0.1}$	59.6	23.5	83.0	16.9
Ni–$Ce_{0.5}Zr_{0.5}$	69.8	16.0	85.8	14.3

[a] Percentages as $O_x/(O_L + O_R)$.

representative Ni–CeZr samples. It is observed that the contribution of O_R (vacancies) and all the lattice oxygen species ($O_L = O_{L1} + O_{L2}$) is very similar for all three cases (ca. 15% of O_R species). However, the ratio between the different types of lattice oxygens is rather different. Thus, O_{L2} is diminished when Zr loading increases whereas the O_{L1} signal followed the opposite trend, which may indicate the formation of CeZr solid solution as deduced from XRD results for the Ni/$Ce_{0.5}Zr_{0.5}$ catalyst.

Regarding the surface nickel, the Ni $2p_{3/2}$ signal was registered and displayed in Figure 5b. NiO spectrum signal of the reference sample was included for comparative purposes (Figure S1). The spectrum of NiO sample consists of three isolated peaks, the one centred at ca. 854 eV assigned to stoichiometric Ni^{2+} species (main peak) and two more peaks at ca. 856 and ca. 861 eV, respectively. The first one (usually called satellite II) at ca. 856 eV has been related to Ni^{2+} vacancies, overoxidized Ni^{3+} species or to non-local screening mechanism.[57–60] The second peak (usually called satellite I) has been also linked to defective species, involving a charge transfer ligand–metal.[57–60] In the case of the NiO–CeO_2 and NiO–CeO_2–ZrO_2 catalysts the same contributions than in pure NiO sample were clearly noticed although slightly blue shifted as a consequence of Ce–Ni or Zr–Ni interaction (Ni electronic transfer to Ce or Zr).[51,61] Comparing the spectra of the three NiO–CeO_2–(ZrO_2) catalysts, it can be observed that the relative intensity of the peaks at 856 and 861 eV (not corresponding to stoichiometric $Ni^{2+}O$ species) compared to the main peak is lowest in the NiO–CeO_2–ZrO_2 catalyst with the lowest Zr-loading: Ni–$Ce_{0.9}Zr_{0.1}$ < Ni–$Ce_{0.5}Zr_{0.5}$ < Ni–Ce. Finally, regarding to

the amount of Ni on the near surface, Table 3 shows that Ni is similarly exposed in all samples and this Ni-loading is higher in the near surface than in the bulk (ca. 0.15 on the near surface vs 0.11 in the bulk).

Ce 3*d* core level spectra for the prepared samples are collected in Figure 5c. Despite the fairly complexity of Ce 3*d* XPS spectra due to the overlapping of spin-doublets, in all the samples the presence of Ce^{3+} and Ce^{4+} species was evidenced, with a greater proportion of Ce^{4+} since the samples were calcined. Ce^{3+} binding energy doublets υ′ and u′ were located at 884.4 eV and 902.7 eV, respectively. Ce^{4+} species showed the spin-orbit doublets and satellite peaks υ (~882.2 eV) and u (~900.6 eV); υ″ (~888.6 eV) and u″ (~907.5 eV); υ‴ (~898.0 eV) and u‴ (~916.4 eV).[51] From the areas of the deconvoluted peaks it is observed that the addition of Zr decreases the proportion of Ce^{3+} species, changing the Ce^{3+}/Ce^{4+} ratio from 0.23 in Ni–Ce sample, to 0.11 for Ni–$Ce_{0.5}Zr_{0.5}$. Moreover, it can be seen that the BEs of Ce^{4+} and Ce^{3+} contributions did not present any red or blue shifts with the incorporation of Zr.[56] Therefore, the presence of Ni leads to an effect, which is inverse to that expected in Ni-free Ce–Zr–O materials. Then, in our catalysts with nickel, the presence of Ce^{3+}, that induces surface defects such as oxygen vacancies and promotes oxygen mobility,[62] is lower for the samples containing Zr.

Lastly, Zr 3*d* XPS spectra are included in Figure 5d and could be deconvoluted into two contributions at 181.5 eV and at 184 eV, related to the split of the spin orbits Zr $3d_{3/2}$ and Zr $3d_{5/2}$, respectively. These values are lower than those reported for pure ZrO_2 (182.5 eV)[63] and those previously reported in Ni–Ce–Zr systems[56] but close to those reported for Ce–Zr systems forming a solid solution,[64,65] which supports XRD findings. It is observed that the signals suffered a red shift of 0.4 eV at the highest Zr loading, which suggests an electron transfer from Ce or Ni to Zr.[61] Moreover, it is reported a BE of 181.5 eV for monoclinic ZrO_2.[66]

Regarding the relative atomic concentrations collected in Table 3, the XPS values suggested that Ni is preferentially located on the catalysts' surface and this enrichment is enhanced with Zr loading. Likewise, Ce/Zr ratio suggests that Ce is also more superficially exposed than Zr.

The morphology of the prepared samples as well as the metallic dispersion was evaluated by means of HR-TEM and selected images are displayed in Figure 6. All samples presented uniform, rounded particles. The particle size distribution evidenced that these catalysts present similar particle size distribution although an increase of the Zr loading provokes a slight decrease in particle size.[67] This unexpected trend, as the increase in the Zr-loading leads to a decrease of the surface area, can be explained by changes in the textural properties observed from N_2 isotherms. Figure 7 shows EDX-STEM mapping graphs with the distribution of Ni, Ce and Zr. In the Ni–Ce catalyst, Figure 7a qualitatively indicates a homogeneous distribution of Ni and Ce, with nickel uniformly spreading on the Ce-matrix (CeO_2). Similarly, the NiO–CeO_2–ZrO_2 samples also show a good distribution of Ni and Ce (Figure 7b and c). However, the presence of Zr agglomerates suggests the formation of ZrO_2. This trend is more notorious in that sample with the highest Zr loading (i.e., Ni–$Ce_{0.5}Zr_{0.5}$). Considering the results obtained by XRD and TEM, it could be proposed that zirconium is present in the Ni–$Ce_{0.5}Zr_{0.5}$ not only as in the Ce–Zr–O solid solution, but also as amorphous ZrO_2. In the case of the catalyst with less Zr (i.e., Ni–$Ce_{0.9}Zr_{0.1}$), zirconium is mainly present in the CeO_2 structure although also in the mixed Ce–Zr-oxide and as amorphous ZrO_2.

Catalytic Study

NiO–CeO_2 and NiO–CeO_2–ZrO_2 catalysts were tested in the N_2O assisted oxidative dehydrogenation of ethane. We want to note that only ethylene and CO_2 have been observed as reaction products.

Using the Ni/Ce catalyst, the selectivity to ethylene at low conversions was over 60% (Figure 8a). Increasing the ethane conversion, part of the olefin was decomposed into CO_2, thus decreasing the selectivity to ethylene when the conversion increased. Similar trend was observed in the NiO–CeO_2–ZrO_2 catalysts although with changes in the selectivity to ethylene, depending on the sample composition. Figure 8b shows the variation of the selectivity to ethylene at isoconversion conditions for NiO–CeO_2 and NiO–CeO_2–ZrO_2 catalysts. Then, the partial replacement of Ce by Zr led to an important increase in the selectivity to ethylene (Figure 8b). In this way, a substitution of 10% of Ce by Zr (Ni/$Ce_{0.9}Zr_{0.1}$) led to the highest improvement in selectivity. However, an excess in the Zr loading meant a further decrease in the olefin formation, obtaining for the Ni/$Ce_{0.5}Zr_{0.5}$ catalyst worse performance than for the Zr-free catalyst (Figure 8a).

Interestingly, the same trend regarding the catalytic activity was observed. Firstly, an increase with the Zr-loading and then a decrease. Thus, the Ni/$Ce_{0.9}Zr_{0.1}$ catalyst was again the most active sample. As this catalyst was the most active and the most

Table 3. Relative atomic concentrations calculated by XPS and nominal ones.

	Ni/Ce		Ni/Zr		Ce/Zr		Ni/(Ce + Zr)		Ni[a]		Ce^{3+}/Ce^{4+}
Catalyst	XPS	Nom	XPS	Nom	XPS	Nom	XPS	Nom	SI/MP	SII/MP	
Ni–Ce	0.15	0.11	–	–	–	–	0.15	0.11	0.95	0.45	0.23
Ni–$Ce_{0.9}Zr_{0.1}$	0.15	0.12	2.12	1.11	21.79	9.00	0.14	0.11	0.89	0.23	0.15
Ni–$Ce_{0.5}Zr_{0.5}$	0.25	0.22	0.42	0.22	2.62	1.00	0.16	0.11	1.21	0.29	0.11

[a] SI/MP: Relative intensity between the peak at ca. 861 eV and the main peak. SII/MP: Relative intensity between the peak at ca. 856 and the main peak.

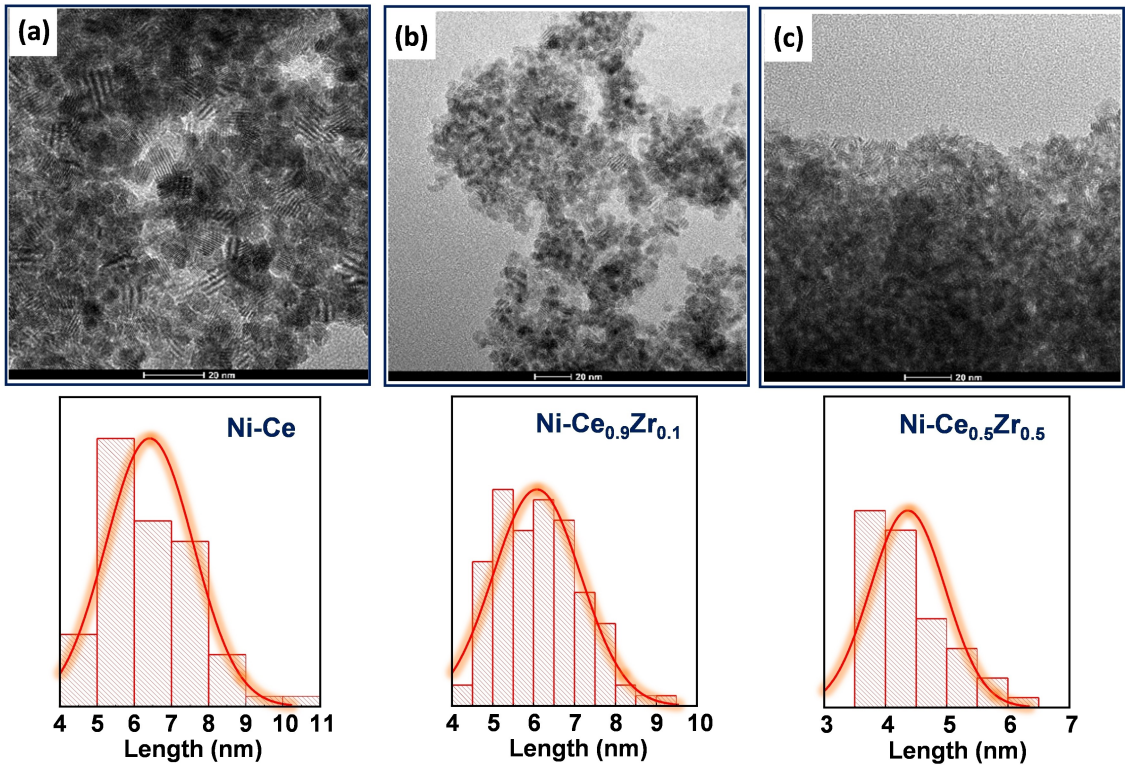

Figure 6. TEM images and particle size distribution for (a) Ni–Ce, (b) Ni–$Ce_{0.9}Zr_{0.1}$ and (c) Ni–$Ce_{0.5}Zr_{0.5}$ samples.

selective, the productivity to ethylene was, by far, the highest among all the catalysts tested.

A more detailed analysis was undertaken with the most efficient catalyst (Ni–$Ce_{0.9}Zr_{0.1}$). In Figure 8c, the variation of the selectivity to ethylene with the ethane conversion at 400 °C using 5% of ethane and different N_2O concentrations was plotted. Although the differences in the curve selectivity vs conversion were not remarkable, for a given conversion it is clearly observed that the higher the N_2O concentration in the feed the lower is the selectivity to the olefin. It seems that these differences lie on the initial formation of the olefin from the alkane rather than to different levels of ethylene overoxidation.

As in the scientific literature the oxidative dehydrogenation of ethane has been mainly studied using molecular oxygen as an oxidizing agent a comparative study between O_2 and N_2O has been also carried out. This comparative study has been undertaken using the same concentration of oxygen atoms (C_2H_6/N_2O/He: 5/10/85 or C_2H_6/O_2/He: 5/5/90 molar ratio). Figure 8d shows that the use of molecular oxygen in the feed favours the ethane transformation, reaching a catalytic activity ca. 3 times that obtained using N_2O. Conversely, the use of N_2O shows, at isoconversion conditions, selectivity to the olefin ca. 15 points higher than when employing O_2. Therefore, although the use of both oxidants presents pros and cons, one could opt by the most selective option, which is that using nitrous oxide. The milder oxidizing character of N_2O compared to O_2 likely induces a lower oxidation state of the active NiO surface. Since overstoichiometric nickel oxide is highly selectivity to carbon oxides,[31] a higher selectivity to ethylene can be obtained by reducing the concentration of oxygen species on the surface of nickel oxide. This trend is similar to that previously reported in vanadium based catalysts.[68] In this case, working at reaction temperatures higher than 500 °C, nitrous oxide reoxidizes the reduced VOx surface species more slowly than molecular oxygen does. This way, surface VOx species are more reduced and the amount of active and unselective oxygen species is lower.

The stability of the optimal catalyst, Ni–$Ce_{0.9}Zr_{0.1}$, was also studied for 8 h at 400 °C. Apparently, no decay neither in the catalytic activity nor in the selectivity to ethylene was observed (Figure S1), corroborating its good stability at least in these conditions. This stable behaviour is consistent with the fact that no changes in the nature of the crystalline phases present (see Figure 4) have been observed after being used. Figure S2 shows additional characterization of the fresh and the used Ni/$Ce_{0.9}Zr_{0.1}$ catalyst, confirming the scarce modification the catalyst has has during the use. Interestingly, no significant changes have been detected after use regarding the surface area (91 vs 89 $m^2 g^{-1}$ for fresh and used catalyst), the mean ceria crystallite size (6.9 and 6.8 nm) and electrochemical characterization (for example, the number of defects is kept stable).

Moreover, different assays were undertaken modifying the relative amounts of ethane and nitrous oxide in order to determine apparent reaction orders (Figure S3 shows a sample of them). The reaction rates as well as the reaction orders have been determined for ethane conversions lower than 10%. Then, the reaction order of the ethane transformation with respect to N_2O resulted to be 0.31 whereas with respect to ethane was

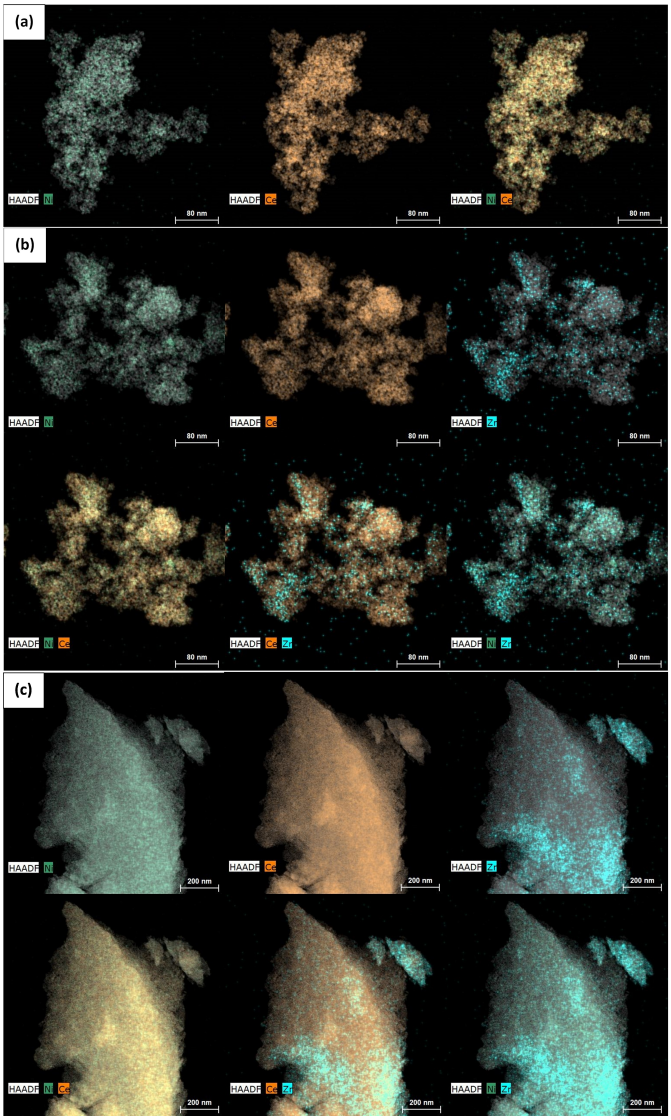

Figure 7. EDX-STEM images showing the distribution of the different chemical elements for (a) Ni–Ce, (b) Ni–$Ce_{0.9}Zr_{0.1}$ and (c) Ni–$Ce_{0.5}Zr_{0.5}$.

0.74. On the other hand, the reaction order of the N_2O transformation with respect to N_2O is 0.43 whereas with respect to ethane is 0.67.

For comparison, the decomposition of N_2O without ethane was also studied (Figure S4) on the most selective sample. Then, it was observed that the presence of ethane does not enhance the N_2O conversion. For example, in comparable conditions at 400 °C the N_2O conversion was ca. 16% with or without ethane. In conditions with high alkane to nitrous oxide ratio it is usual a positive role of the alkane, due to its reducing character.[69] However, in the present article not a significant effect has been observed, maybe due to the low alkane to nitrous oxide ratio (0.5) employed.

Relationship Between the Electrochemical Properties, the Physico-Chemical Characterization and the Catalytic Results

Following, an electrochemical study was conducted to find a relationship with the characterization previously made and, especially, with the catalytic results in the ODH-N_2O of ethane. Thus, electrochemical response of representative NiO–CeO_2–(ZrO_2) catalysts (Ni–Ce, Ni–$Ce_{0.9}Zr_{0.1}$ and Ni–$Ce_{0.5}Zr_{0.5}$) was studied through Electrochemical Impedance Spectroscopy (EIS) and Mott-Schottky (MS) analyses. Figure 9 shows the Nyquist (A) and Bode (B) plots. Bode diagram clearly shows two time constants for all the studied catalysts, which are related to two unfinished semicircles in the Nyquist chart, one at low frequencies and the other at medium/high ones. Bode module plot presents at low frequencies the total resistances of the catalysts, i.e., the corresponding to the bulk oxide (mainly composed by ceria or ceria-zirconium mixed oxide) plus the catalytic oxide layer (nickel oxide + cerium/zirconium oxides). According to this, the lowest R_T values are obtained for the Ni/Ce sample. However, an equivalent circuit in series (see inset of Figure 9a) was used to better correlate electrochemical properties of the samples with catalytic ones. The circuit was formed by the electrochemical resistance to the electrolyte (Rs, which was constant for all the experiments, see |Z| values of Figure 9b at high frequencies) and two constant phase element/resistant groups (CPE–R) disposed in parallel. The first CPE–R group was associated with the outer catalytic oxide layer, thus, R_1 corresponding to the charge transfer resistance of the sample. On the other hand, the second CPE–R component was related to the cerium oxide bulk of the catalysts (or cerium + zirconium oxides for the Ni–$Ce_{0.5}Zr_{0.5}$ sample). CPEs were used in order to take into consideration the heterogeneities of the catalytic system.[70]

As shown in Figure 9a (see table inside), R_1 values are similar regardless of the catalyst. Nevertheless, according to Bode phase plots, some differences can be appreciated, that is, higher phase angles (~80°) are obtained for the Ni–$Ce_{0.9}Zr_{0.1}$ catalyst respect to the circa 60° of the Ni–Ce sample. Therefore, a more homogeneous and non-defective inner Ce oxide layer might be decisive in the catalytic character of the samples; hence, related to higher selectivity to the desired product.

Figure 10 shows the Mott-Schottky plots obtained for the different studied catalysts. In all cases, a positive slope can be elucidated, which was associated with a n-type semiconductivity. Hence, as expected, the presence of low amount of nickel oxide ((Ce + Zr)/Ni = 9 at.) does not change the typical n-type character of the Ce or Ce/Zr oxides.

In oxides showing n-type semiconductive character, oxygen vacancies (V_O^X) are the prevailing defects. From the slopes of the MS plots, the concentration of oxygen vacancies can be calculated (see Table in Figure 10), according to Equation (1):

$$N_D = \frac{2}{\varepsilon \cdot \varepsilon_0 \cdot e \cdot \sigma} \quad (1)$$

where ε is the dielectric constant of the CeO_2 (25.0)[18,71–73] or the ZrO_2 (19.5)[74] in its appropriated ratio, ε_0 is the vacuum

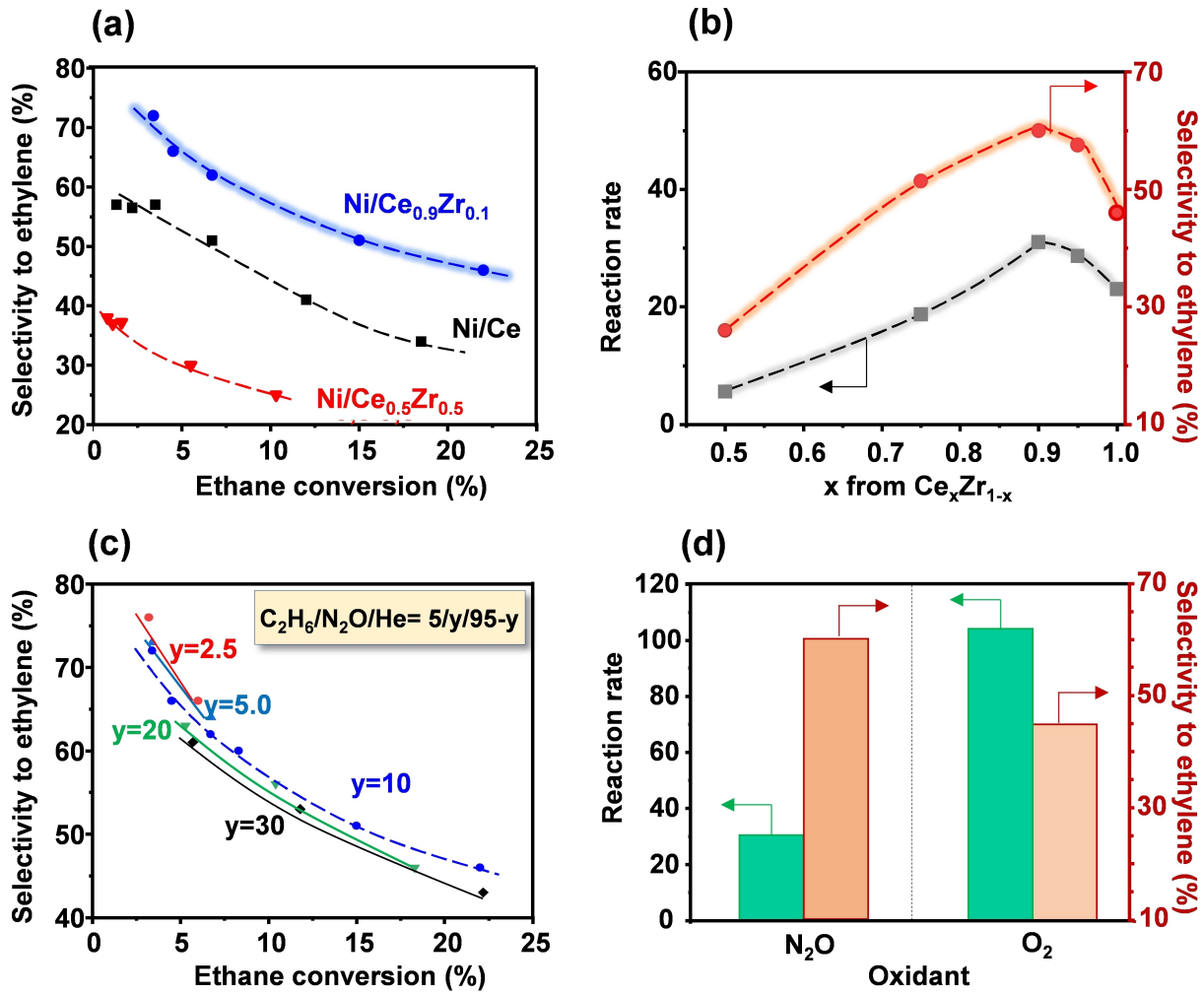

Figure 8. (a) Evolution of the selectivity to ethylene with the ethane conversion at 400 °C with a feed consisting of C_2H_6/N_2O/He: 5/10/85 molar ratio and using different contact times. Symbols: (■ black) Ni–Ce, (● blue) Ni–$Ce_{0.9}Zr_{0.1}$, (▼ red) Ni–$Ce_{0.5}Zr_{0.5}$. (b) (left, ■ grey) Relationship between the Ce/(Ce + Zr) ratio and the reaction rate (in $g_{C2H6}\ kg_{cat}^{-1}\ h^{-1}$ determined at 400 °C, C_2H_6/N_2O/He : 5/10/85 molar ratio, 80 $g_{cat}\ h\ mol_{C2H6}^{-1}$); (right, ● red) influence of the Ce/(Ce + Zr) ratio on the selectivity to ethylene (400 °C, C_2/N_2O/He : 5/10/85 molar ratio, isoconversion of 10%). (c) Evolution of the selectivity to ethylene with the ethane conversion at 400 °C with a feed consisting of C_2H_6/N_2O/He: 5/y/95-y molar ratio and using different contact times for the Ni–$Ce_{0.9}Zr_{0.1}$ catalyst. (d) (left) Reaction rate using N_2O (C_2H_6/N_2O/He: 5/10/85 molar ratio) or O_2 (C_2H_6/O_2/He: 5/5/90 molar ratio) as oxidizing agents (in $g_{C2H6}\ kg_{cat}^{-1}\ h^{-1}$ determined at 400 °C and a contact time of 80 $g_{cat}\ h\ mol_{C2H6}^{-1}$); (right) Selectivity to ethylene using N_2O (C_2H_6/N_2O/He: 5/10/85 molar ratio) or O_2 (C_2H_6/O_2/He: 5/5/90 molar ratio) as oxidizing agents (400 °C, isoconversion of 10%).

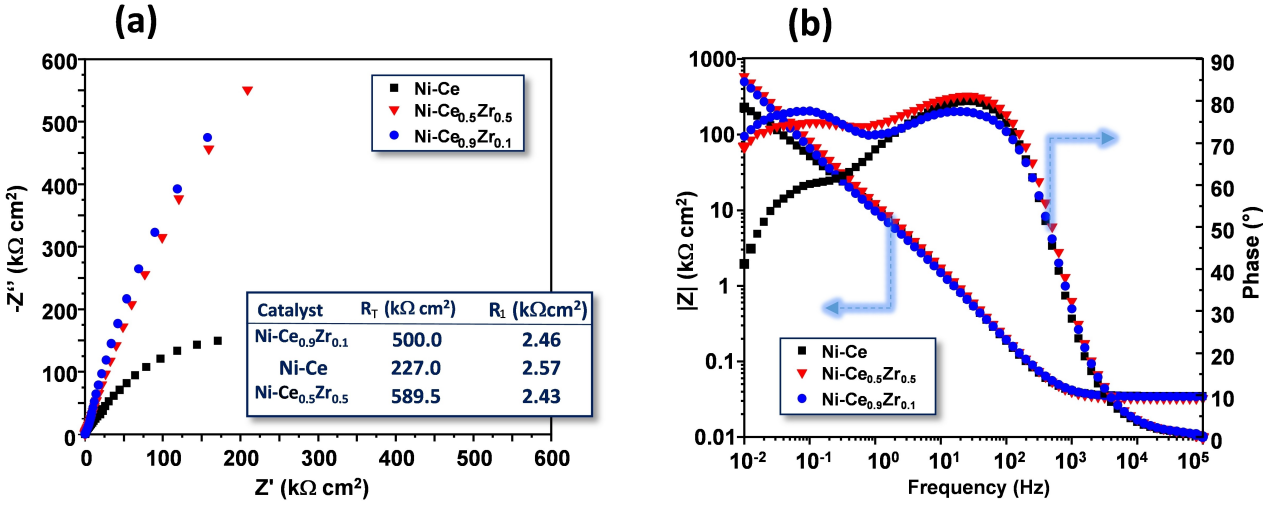

Figure 9. Nyquist (a) and Bode (b) plots for the different Ni–CeO_2–ZrO_2 catalysts.

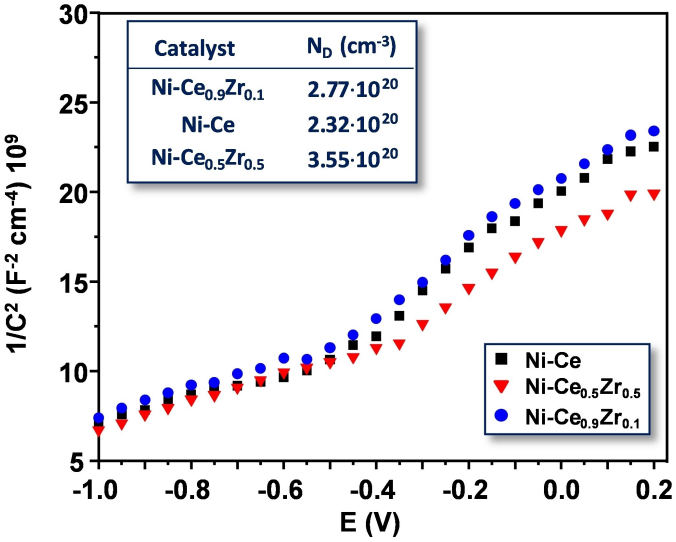

Figure 10. Mott-Schottky plots for the different Ni–Ce and Ni–CeZr catalysts.

permittivity (8.85×10^{-14} F cm^{-1}), e is the electron charge (1.60×10^{-19} C) and σ is the positive slope of each straight line in MS plots. According to this, the number of oxygen vacancies was higher for the Ni/$Ce_{0.5}Zr_{0.5}$ sample, whereas the lower concentration of defects was shown for the sample containing the lowest amount of Zr (Ni–$Ce_{0.9}Zr_{0.1}$).

Interestingly, there is an inverse correlation between selectivity to ethylene in ODH reaction and the concentration of oxygen vacancies, that can be explained as follows. V_O^X are created from the transfer of an oxygen atom in a normal site of the lattice (O^{2-}/O_O^X) to the gaseous state, as shown in Equation (2):

$$O_O^X \rightarrow V_O^X + 2e^- + \frac{1}{2}O_2 \quad (2)$$

Therefore, a competition between nucleophilic oxygen species (O^{2-}/O_O^X), responsible for the enhancement of the selectivity to ethylene, and oxygen vacancies, occurred. Thus, a high concentration of oxygen vacancies (Ni–$Ce_{0.5}Zr_{0.5}$) leads to lower selectivity to ethylene in comparison to the Ni/$Ce_{0.9}Zr_{0.1}$ catalyst, which presented a much lower number of defects (2.77×10^{20} compared to 3.55×10^{20} cm^{-3}, respectively).

In previous articles, it was demonstrated that, in the oxidative dehydrogenation of ethane using oxygen as an oxidizing agent over doped nickel oxide catalysts, there exists an inverse relationship between the density of non-stoichiometric oxygen and the selectivity towards ethylene. Thus, decreasing the p-character of the catalysts the ethylene formation can be enhanced.[75–78] Interestingly, recently, in the same reaction with molecular oxygen, it was observed that completely removing the p-character, the highest selectivity to ethylene could be obtained. In fact, a NiO doped catalyst suitably synthesized that posed a slight n-character achieved the highest selectivity among a set of catalysts.[75] Accordingly, in the present article, we have wanted to determine the positive or negative influence of the presence of oxygen vacancies. Then, considering that all the catalysts present overall n-type conductivity, we have observed that the most selective catalyst to ethylene is the one that presents the lowest concentration of surface defects (oxygen vacancies).

However, we have to consider that the active and selective sites in the N_2O-assisted ethane ODH are those of nickel. In fact, pure cerium oxide is poorly active and, besides, unselective towards the formation of ethylene.[25] Therefore, the direct role of cerium oxide sites for ethane oxidation is not so important. Importantly, that catalyst with the lowest concentration of defective nickel surface sites on the near surface is that with the lowest amount of Zr (i.e., Ni–$Ce_{0.9}Zr_{0.1}$ catalyst), which is the most selective towards the formation of ethylene.

On the other hand, the catalyst with only ceria presents the highest concentration of non-stoichiometric surface Ce^{3+} determined by XPS, related to the surface oxygen vacancies, which is detrimental for the ethylene formation. Conversely, the electrochemical study (see Mott-Schottky plot) indicates that the sample with more surface defects is that with the highest amount of Zr (i.e., Ni–$Ce_{0.5}Zr_{0.5}$ catalyst). This apparently contradictory results can be explained by the fact that in the Ni–CeZr catalysts the whole surface does not consist only of ceria but also of nickel (and zirconium) sites and the electrochemical study takes into account all the oxygen vacancies, not only those surrounding cerium. Moreover, the role of nickel on the surface is especially important as it is the most active catalytic site and its near surface concentration is remarkably higher (ca. 40%) than that in the bulk (Table 3).

Overall, it has been observed that the addition of Zr in appropriate amounts to a NiO–CeO_2 sample enhances the selectivity to olefin compared to the Zr-free NiO–CeO_2 catalyst in the oxidative dehydrogenation of ethane using N_2O as an oxidizing agent. The lower formation of unselective non-stoichiometric species (cationic defective sites of nickel and the anionic ceria sites) is likely the reason for the enhanced selectivity to ethylene of Ni–$Ce_{0.9}Zr_{0.1}$ catalyst.

Finally, we want to mention that, in the present article, a combined reaction involving the selective transformation of ethane and the decomposition of N_2O has been studied and, importantly, the use of a gas with high potential for global warming as N_2O, has led to a remarkable increase in the ethylene selectivity (ca. 15% upper) compared to the analogous reaction with molecular oxygen.

Conclusions

NiO–CeO_2 and NiO–CeO_2–ZrO_2 are active and selective catalysts to ethylene in the N_2O assisted oxidative dehydrogenation (ODH) of ethane. The best catalytic results have been obtained when the support is CeO_2–ZrO_2 with low Zr/Ce ratio. The improved performance of the optimal catalyst, that corresponds to a Zr/Ce at. ratio of 0.1, is related to the scarce formation of unselective cationic defective surface sites of nickel. An excess of Zr has meant a worsening of the selectivity to ethylene likely due to an increase in the formation of non-stoichiometric

species (more defective nickel surface species and an increase in the global n semiconductivity). We want to indicate that the optimal catalyst is highly stable at least for 8 h on-line and no apparent changes in the activity or in the selectivity has been observed. Accordingly, hardly variations in the surface area, the crystalline phases present or the crystallite size have been observed after use. Interestingly, the N_2O assisted ODH of ethane has resulted to be more selective to the olefin than the O_2 assisted ODH of ethane, although the catalytic activity is higher if molecular oxygen is used as an oxidizing agent.

Experimental Section

Characterization Techniques

Nitrogen adsorption-desorption isotherms were conducted at −196 °C using a Micromeritics ASAP 2020 apparatus. Before analysis, the samples were outgassed at 150 °C. The specific surface area was determined using the Brunauer-Emmet-Teller (BET) method. Pore volume was assessed at a relative pressure of $P/P_0 =$ 0.94, and the pore size distribution was determined through the DFT method.

X-ray diffraction patterns were recorded with a *PANalytical CUBIX* instrument equipped with a graphite monochromator, by using Cu Kα radiation (λ = 0.1542 mm) and operating at 45 kV and 4 mA.

High resolution TEM images were collected with a TALOS F200x microscope working at 5.5 μA and 200 kV. EDX-STEM mapping was performed using a HAADF detector working at 200 pA and 200 kV.

XPS analysis was performed in a PHI 5700 Physical Electronics spectrometer, with X-ray monochromatic source Al Kα of photons at 1486.6 eV under ultra-high vacuum and equipped with a multichannel detector. PHI ACCESS ESCA–V6.0 F software was used to collect spectra using a constant step mode of 29.35 eV. C 1s peak of adventitious carbon contamination layer (284.8 eV) was used for charge correction and the estimated error in binding energy values was ±0.1 eV. Multipak 9.5 software was used for data analysis.

Electrochemical Characterization

Electrochemical interfacial properties of the catalysts were studied in a three-electrode electrochemical cell with an Ag/AgCl 3 M KCl reference electrode and a platinum wire as counter electrode. The catalysts were connected to the potentiostat as working electrodes with 0.5 cm^2 of exposed area to the electrolyte. Mott-Schottky (MS) measurements and Electrochemical Impedance Spectroscopy (EIS) tests were carried out to characterize the catalysts, specifically their electrochemical properties at the interface between the catalysts (working electrodes) and the electrolyte. Mott-Schottky plots were performed at a frequency of 5000 Hz, scanning the potential from 0.2 to −1 VAg/AgCl at 0.05 V/s using an amplitude signal of 0.01 V. Before EIS measurements, catalysts were immersed in the solution for 1800 s at 0 VAg/AgCl. After this pre-treatment, EIS tests were carried out applying a potential of 0 VAg/AgCl using an amplitude of 0.01 V and scanning frequencies from 100 kHz to 0.01 Hz. The electrolyte used was 0.1 M of $Na_2(SO)_4$.

Catalysts Synthesis

The catalysts were prepared by coprecipitation. Ni–CeO_2–ZrO_2 catalysts with (Ce + Zr)/Ni molar ratio of 9 and Zr/Ce at. ratios of 0.05, 0.1, 0.25 and 0.5 were prepared by dissolution of the calculated amount of $Ni(NO_3)_2 \cdot 6H_2O$ (Sigma-Aldrich, 99.99%), $Ce(NO_3)_3 \cdot 6H_2O$ (Sigma-Aldrich, 99.99%) and $ZrO(NO_3)_3 \cdot xH_2O$ (Aldrich, 99%) in 100 mL of distilled water. NaOH and Na_2CO_3 were used as precipitating agents. A Na_2CO_3 0.1 M and NaOH 0.5 M solution was added dropwise over the prepared solution under vigorous stirring at room temperature and pH was stabilized at 10 for 30 min. Afterwards, the samples were filtered under vacuum and washed to remove Na. Lastly, the samples were calcined at 400 °C for two hours with a heating rate of 5 °C min^{-1}. The samples were labelled as Ni–Ce (sample without Zr), Ni–$Ce_{0.95}Zr_{0.05}$, Ni–$Ce_{0.9}Zr_{0.1}$, Ni–$Ce_{0.75}Zr_{0.75}$ and Ni–$Ce_{0.5}Zr_{0.5}$ (for Zr/Ce at. ratios of 0.05, 0.1, 0.25 and 0.5, respectively). Three representative catalysts of this set were chosen for a deep characterization study: the base Zr-free (Ni–Ce), the optimal (Ni–$Ce_{0.9}Zr_{0.1}$) and the least selective catalyst (Ni–$Ce_{0.5}Zr_{0.5}$).

Pure NiO or pure CeO_2 were prepared just calcining the precursors $Ni(NO_3)_2 \cdot 6H_2O$ (Sigma-Aldrich, 99.99%) or $Ce(NO_3)_3 \cdot 6H_2O$ (Sigma-Aldrich, 99.99%) in static air at 400 °C for 2 h. These catalysts were tested in the N_2O-ODH achieving for both cases low selectivity to the olefin (for any conversion, the selectivity to ethylene was lower than 30% and 8% for pure NiO and CeO_2 respectively).

Catalytic Tests in Ethane ODH

The N_2O-assisted oxidative dehydrogenation of ethane was conducted in an isothermal fixed-bed quartz reactor working at atmospheric pressure, in the 300–400 °C range, mainly at 400 °C. The feed consisted of a mixture containing ethane, N_2O and helium with variable proportions, but mainly using $C_2H_6/N_2O/He$: 5/10/85 molar ratio. The total flow and the catalyst weight were changed (20–100 mL min^{-1} and 0.1–1.2 g of catalyst) to get different conversion levels. For a comparative purpose, tests using molecular oxygen as an oxidizing agent were also carried out (C_2H_6/O_2/He: 5/5/90 molar ratio). Reactants and products were analyzed by gas chromatography using two packed columns: (i) molecular sieve 5 A (2.5 m); and (ii) Porapak Q (3 m).

Supporting Information Summary

The authors have included additional Figures within the Supporting Information.

Acknowledgements

The authors would like to acknowledge the Ministerio de Ciencia e Innovación-Agencia Estatal de Investigación through the projects PID2021-126235OB-C31, PID2021-126235OB-C32 and PID2021–126235OB-C33 (funded by MCIN/AEI/10.13039/501100011033 and FEDER funds), and TED2021-129555B-I00/AEI/10.13039/501100011033/Unión Europea NextGenerationEU/PRTR. The authors also thank the Generalitat Valenciana for CIAICO/2021/094 and CIGRIS/2022/198.

Conflict of Interests

The authors declare no conflict of interest.

Data Availability Statement

The data that support the findings of this study are available from the corresponding author upon reasonable request.

Keywords: ODH of ethane · N_2O · Ni–Ce–Zr–O catalysts · Semiconductivity · Ni surface species

[1] EPA, "Overview of Greenhouse Gases," can be found under https://www.epa.gov/ghgemissions/overview-greenhouse-gases.
[2] IPCC, "Climate Change 2021: The Physical Science Basis," can be found under https://www.ipcc.ch/report/ar6/wg1/.
[3] E. W. R. Steacie, R. D. McDonald, *Can. J. Res.* **1935**, *12*, 711–714.
[4] S. Impeng, T. Roongcharoen, P. Maitarad, H. Wu, C. Chitpakdee, V. Promarak, L. Shi, S. Namuangruk, *Appl. Surf. Sci.* **2020**, *513*, 145799.
[5] V. D. B. C. Dasireddy, D. Hanzel, K. Bharuth-Ram, B. Likozar, *RSC Adv.* **2019**, *9*, 30989–31003.
[6] Z. Liu, X. Sun, Y. Li, Z. Sui, X. Xu, *J. Environ. Chem. Eng.* **2022**, *10*, 108609.
[7] F. Trifirò, I. Pasquon, *J. Catal.* **1968**, *12*, 412–416.
[8] B. Solsona, P. Concepción, B. Demicol, S. Hernández, J. J. Delgado, J. J. Calvino, J. M. López Nieto, *J. Catal.* **2012**, *295*, 104–114.
[9] E. Heracleous, A. A. Lemonidou, *J. Catal.* **2006**, *237*, 162–174.
[10] X. Zhao, M. D. Susman, J. D. Rimer, P. Bollini, *Catal. Sci. Technol.* **2021**, *11*, 531–541.
[11] Y. Abdelbaki, A. de Arriba, R. Issaadi, R. Sánchez-Tovar, B. Solsona, J. M. López Nieto, *Fuel Process. Technol.* **2022**, *229*, 107182.
[12] Ş. B. Ivan, I. Fechete, F. Papa, I. C. Marcu, *Catal. Today* **2021**, *366*, 133–140.
[13] D. Delgado, B. Solsona, R. Sanchis, E. Rodríguez-Castellón, J. M. López Nieto, *Catal. Today* **2021**, *363*, 27–35.
[14] Z. Skoufa, E. Heracleous, A. A. Lemonidou, *J. Catal.* **2015**, *322*, 118–129.
[15] J. L. Park, K. A. Canizales, M. D. Argyle, B. F. Woodfield, K. J. Stowers, *Microp. Mesop. Mat.* **2020**, *293*, 109799.
[16] L. Smoláková, M. Kout, L. Čapek, *Top. Catal.* **2015**, *58*, 843–853.
[17] J. L. Park, S. K. Balijepalli, M. D. Argyle, K. J. Stowers, *Ind. Eng. Chem. Res.* **2018**, *57*, 5234–5240.
[18] A. García, L. Toca, R. M. Fernández-Domene, F. Ivars-Barceló, E. Montejano-Nares, P. Amorós, R. Sánchez-Tovar, B. Solsona, *Appl. Surf. Sci.* **2024**, *653*, 159354.
[19] A. Trovarelli, J. Llorca, *ACS Catal.* **2017**, *7*, 4716–4735.
[20] Z. A. Qiao, Z. Wu, S. Dai, *ChemSusChem* **2013**, *6*, 1821–1833.
[21] C. T. Campbell, C. H. F. Peden, *Science* **2005**, *309*, 713–714.
[22] Z. Li, B. S. Haynes, A. Montoya, *ACS Appl. Mater. Interfaces* **2023**, *15*, 51885–51893.
[23] H. J. Kim, M. G. Jang, D. Shin, J. W. Han, *ChemCatChem* **2020**, *12*, 11–26.
[24] H. J. Kim, M. G. Jang, D. Shin, J. W. Han, *ChemCatChem* **2020**, *12*, 1.
[25] B. Solsona, P. Concepción, S. Hernández, B. Demicol, J. M. López Nieto, *Catal. Today* **2012**, *180*, 51–58.
[26] L. Alves, L. I. V. Holz, C. Fernandes, P. Ribeirinha, D. Mendes, D. P. Fagg, A. Mendes, *Renewable Sustainable Energy Rev.* **2022**, *155*, 111916.
[27] Y. K. Park, B. S. Kim, *Chem. Eng. J.* **2023**, *461*, 141958.
[28] J. Pérez-Ramírez, F. Kapteijn, K. Schöffel, J. A. Moulijn, *Appl. Catal. B* **2003**, *44*, 117–151.
[29] M. Konsolakis, *ACS Catal.* **2015**, *5*, 6397–6421.
[30] T. Yamashita, A. Vannice, *J. Catal.* **1996**, *161*, 254–262.
[31] B. M. Abu-Zied, S. A. Soliman, S. E. Abdellah, *Chin. J. Catal.* **2014**, *35*, 1105.
[32] P. H. Ho, M. Jabłońska, G. Beltrami, A. Martucci, T. Cacciaguerra, W. Paulus, F. Di Renzo, G. Fornasari, A. Vaccari, P. Benito, R. Palkovits, *J. Mater. Sci.* **2021**, *56*, 15012–15028.
[33] J. Qi, X. Qi, Y. Pan, J. Cui, Y. Xiong, W. Shan, H. Yu, *Appl. Surf. Sci.* **2023**, *611*, 155657.
[34] F. Pan, B. Li, W. Deng, Z. Du, Y. Gang, G. Wang, Y. Li, *Appl. Catal. B* **2019**, *252*, 240–249.
[35] F. Zhang, X. Wang, X. Zhang, M. Turxun, H. Yu, J. Zhao, *Chem. Eng. J.* **2014**, *256*, 365–371.
[36] P. Zhao, F. Qin, Z. Huang, C. Sun, W. Shen, H. Xu, *Chem. Eng. J.* **2018**, *349*, 72–81.
[37] Z. Liu, Z. Zhou, F. He, B. Chen, Y. Zhao, Q. Xu, *Catal. Today* **2017**, *293–294*, 56–60.
[38] H. F. Wang, X. Q. Gong, Y. L. Guo, Y. Guo, G. Z. Lu, P. Hu, *J. Phys. Chem. C* **2009**, *113*, 10229–10232.
[39] G. S. Otero, P. G. Lustemberg, F. Prado, M. V. Ganduglia-Pirovano, *J. Phys. Chem. C* **2020**, *124*, 625–638.
[40] P. T. Aragão Campos, C. F. Oliveira, J. P. Vieira Lima, D. Renata de Queiroz Silva, S. C. Loureiro Dias, J. A. Dias, *J. Solid State Chem.* **2022**, *307*, 122752.
[41] O. Ovsitser, E. V. Kondratenko, *Catal. Today* **2009**, *142*, 138–142.
[42] X. Rozanska, E. V. Kondratenko, J. Sauer, *J. Catal.* **2008**, *256*, 84–94.
[43] A. Held, J. Kowalska, K. Nowińska, *Appl. Catal. B* **2006**, *64*, 201–208.
[44] Y. Zhou, J. Lin, L. Li, M. Tian, X. Li, X. Pan, Y. Chen, X. Wang, *J. Catal.* **2019**, *377*, 438–448.
[45] M. A. Behnajady, S. Bimeghdar, *Chem. Eng. J.* **2014**, *239*, 105–113.
[46] M. Thommes, K. Kaneko, A. V Neimark, J. P. Olivier, F. Rodriguez-Reinoso, J. Rouquerol, K. S. W. Sing, *Pure Appl. Chem.* **2015**, *87*, 1051–1069.
[47] G. Zhou, S. Xu, Y. Li, Q. Jiang, B. Xu, H. Xie, G. Zhang, *ChemNanoMat* **2022**, *8*, e202100533.
[48] J. A. Díaz-Guillén, C. Bocardo-Roldán, J. C. Díaz-Guillén, A. F. Fuentes, K. P. Padmasree, *Int. J. Hydrogen Energy* **2024**. DOI: 10.1016/J.IJHYDENE.2024.01.003.
[49] C. Larese, M. López Granados, R. Mariscal, J. L. G. Fierro, P. S. Lambrou, A. M. Efstathiou, *Appl. Catal. B* **2005**, *59*, 13–25.
[50] F. M. Sun, C. F. Yan, Z. Da Wang, C. Q. Guo, S. L. Huang, *Int. J. Hydrogen Energy* **2015**, *40*, 15985–15993.
[51] L. Xu, X. Wen, M. Chen, C. Lv, Y. Cui, X. Wu, C. e. Wu, B. Yang, Z. Miao, X. Hu, *Fuel* **2020**, *282*, 118813.
[52] S. Tong, M. Zheng, Y. Lu, Z. Lin, J. Li, X. Zhang, Y. Shi, P. He, H. Zhou, *J. Mater. Chem. A Mater.* **2015**, *3*, 16177–16182.
[53] M. A. Peck, M. A. Langell, *Chem. Mater.* **2012**, *24*, 4483–4490.
[54] L. A. do Nascimento, L. Barroso-Martín, S. R. S. Peçanha, S. Arias, B. S. Santos, J. G. A. Pacheco, A. Infantes-Molina, E. Rodríguez-Castellón, I. de C. L. Barros, *Catal. Today* **2022**, *394–396*, 282–294.
[55] T. Bao, H. Zhou, Y. Zhang, C. Guo, W. Guo, H. Qin, P. Gao, H. Xiao, W. Liu, *J. Rare Earth* **2023**, *41*, 1703–1713.
[56] M. Chen, X. Feng, Y. Wang, D. Liang, C. Li, Z. Yang, J. Wang, *Fuel* **2023**, *346*, 128373.
[57] M. Tomellini, *J. Chem. Soc. Faraday Trans. 1* **1988**, *84*, 3501–3510.
[58] J. C. Vedrine, G. Hollinger, T. M. Duc, *J. Phys. Chem.* **1978**, *82*, 1515–1520.
[59] M. A. Van Veenendaal, G. A. Sawatzky, *Phys. Rev. Lett.* **1993**, *70*, 2459.
[60] V. Biju, M. Abdul Khadar, *J. Nanopart. Res.* **2002**, *4*, 247–253.
[61] X. Zhou, Y. Gao, J. Yang, W. Yi, Q. Pang, Z. Liu, B. Liu, M. Zhang, *Chem. Eng. Res. Des.* **2023**, *193*, 626–640.
[62] A. S. Al-Fatesh, Y. Arafat, S. O. Kasim, A. A. Ibrahim, A. E. Abasaeed, A. H. Fakeeha, *Appl. Catal. B* **2021**, *280*, 119445.
[63] B. M. Reddy, B. Chowdhury, P. G. Smirniotis, *Appl. Catal. A* **2001**, *211*, 19–30.
[64] A. Galtayries, R. Sporken, J. Riga, G. Blanchard, R. Caudano, *J. Electron Spectrosc. Relat. Phenom.* **1998**, *88–91*, 951–956.
[65] A. V. Paladino Lino, C. B. Rodella, E. M. Assaf, J. M. Assaf, *Int. J. Hydrogen Energy* **2020**, *45*, 8418–8432.
[66] P. Lackner, Z. Zou, S. Mayr, U. Diebold, M. Schmid, *Phys. Chem. Chem. Phys.* **2019**, *21*, 17613–17620.
[67] M. Zhang, X. Zhou, J. Yang, T. Yang, Z. Liu, Y. Han, *Fuel* **2023**, *349*, 128705.
[68] X. Rozanska, E. V. Kondratenko, J Sauer, *J. Catal.* **2008**, *256*, 84–94.
[69] V. A. Kondratenko, T. Hahn, E. V. Kondratenko, *ChemCatChem* **2012**, *4*, 408–414.
[70] S. M. Gateman, O. Gharbi, H. Gomes de Melo, K. Ngo, M. Turmine, V. Vivier, *Curr. Opin. Electrochem.* **2022**, *36*, 101133.
[71] N. Iyer Santha, M. Thomas Sebastian, P. Mohanan, N. McN Alford, K. Sarma, R. C. Pullar, S. Kamba, A. Pashkin, P. Samukhina, J. Petzelt, *J. Am. Ceram. Soc.* **2004**, *87*, 1233–1237.
[72] N. Pradhani, P. K. Mahapatra, R. N. P. Choudhary, *J. Phys. Mater.* **2018**, *1*, 015007.
[73] P. Meléndez-González, M. Esther Sánchez-Castro, I. Liliana Alonso-Lemus, F.-C. Chiu, C.-M. Lai, *J. Phys. D* **2010**, *43*, 075104.

[74] Y. Oh, V. Bharambe, B. Mummareddy, J. Martin, J. McKnight, M. A. Abraham, J. M. Walker, K. Rogers, B. Conner, P. Cortes, E. MacDonald, J. J. Adams, *Addit. Manuf.* **2019**, *27*, 586–594.
[75] I. Popescu, E. Heracleous, Z. Skoufa, A. Lemonidou, I. C. Marcu, *Phys. Chem. Chem. Phys.* **2014**, *16*, 4962–4970.
[76] I. Popescu, Z. Skoufa, E. Heracleous, A. Lemonidou, I. C. Marcu, *Phys. Chem. Chem. Phys.* **2015**, *17*, 8138–8147.
[77] Y. Abdelbaki, R. Sánchez-Tovar, A. de Arriba, E. García-González, R. Fernández-Domene, B. Solsona, J. M. López Nieto, *J. Catal.* **2023**, *420*, 9–22.
[78] J. M. López Nieto, B. Solsona, R. K. Grasselli, P. Concepción, *Top. Catal.* **2014**, *57*, 1248–1255.

Manuscript received: February 16, 2024
Revised manuscript received: July 16, 2024
Accepted manuscript online: August 16, 2024
Version of record online: October 19, 2024